Computer Modeling in
Engineering & Sciences

Tech Science Press

Doi:10.32604/cmes.2025.073292

ARTICLE

Artificial Neural Network-Based Flow and Heat Transfer Analysis of Williamson Nanofluid over a Moving Wedge: Effects of Thermal Radiation, Viscous Dissipation, and Homogeneous-Heterogeneous

Adnan Ashique[1], **Nehad Ali Shah**[1], **Usman Afzal**[1], **Yazen Alawaideh**[2], **Sohaib Abdal**[3] and **Jae Dong Chung**[1,*]

[1]Department of Mechanical Engineering, Sejong University, Seoul, 05006, Republic of Korea
[2]Applied Science Research Center, Applied Science Private University, Amman, 11931, Jordan
[3]Department of Mathematical Sciences, Saveetha School of Engineering, SIMATS, Chennai, 602105, Tamilnadu, India

*Corresponding Author: Jae Dong Chung. Email: jdchung@sejong.ac.kr

Received: 15 September 2025; Accepted: 26 December 2025; Published: 26 February 2026

ABSTRACT: There is a need for accurate prediction of heat and mass transfer in aerodynamically designed, non-Newtonian nanofluids across aerodynamically designed, high-flux biomedical micro-devices for thermal management and reactive coating processes, but existing work is not uncharacteristically remiss regarding viscoelasticity, radiative heating, viscous dissipation, and homogeneous–heterogeneous reactions within a single scheme that is calibrated. This research investigates the flow of Williamson nanofluid across a dynamically wedged surface under conditions that include viscous dissipation, thermal radiation, and homogeneous-heterogeneous reactions. The paper develops a detailed mathematical approach that utilizes boundary layers to transform partial differential equations into ordinary differential equations using similarity transformations. RK4 is the technique for gaining numerical solutions, but with the addition of ANNs, there is an improvement in prediction accuracy and computational efficiency. The study investigates the influence of wedge angle parameter, along with Weissenberg number, thermal radiation parameter and Brownian motion parameter, and Schmidt number, on velocity distribution, temperature distribution, and concentration distribution. Enhanced Weissenberg numbers enhance viscoelastic responses that modify velocity patterns, but radiation parameters and thermophoresis have key impacts on thermal transfer phenomena. This research develops findings that are of enormous application in aerospace, biomedical (artificial hearts and drug delivery), and industrial cooling technology applications. New findings on non-Newtonian nanofluids under full flow systems are included in this work to enhance heat transfer methods in novel fluid-based systems.

KEYWORDS: Williamson fluid; thermal radiation; viscous dissipation; Artificial Neural Networks (ANNs); homogeneous-heterogeneous reactions

1 Introduction

The study of non-Newtonian fluids is of interest to many scientists considering their relevance in everyday life, in mechanical and synthetic processes, biological fluids, pastes, polymeric liquids, complex mixtures, and motor oils [1]. The Williamson fluid model is a non-Newtonian fluid exhibiting pseudoplastic behavior. Pseudoplastic fluids exhibit an immediate reduction in fluid thickness with an increase in shear rate. Salahuddin et al. [2] studied the magnetohydrodynamic (MHD) flow of Williamson nanofluid over stretched surfaces with special emphasis on combined thermal and solutal transport mechanics. Through numerical analysis, Salahuddin and Awais [3] studied how parameter changes affected the distribution of velocity and temperature along with concentration fields. Sankari et al. [4] investigated adding nanoparticles and microorganisms to Williamson fluids while evaluating their influence on stability, together with environmental considerations. The study of Couette flows of a Maxwell fluid that is moved by a flat plate was explained under the slip condition of the boundaries, as illustrated by Vieru and Zafar [5]. Bilal Arain et al. [6] studied bubble dynamics within Williamson fluids under acoustic wave influences to show how group modulations affect radial motions through studies of Reynolds number and magnetic field strengths. Nadeem et al. [7] investigated entropy generation in MHD channel flows of Williamson fluids, which used mixed convective-radiative boundary conditions. Shafiq et al. [8] analyzed that the concentration field and intensity of temperature of Walter's B nonfluid flow are diminished corresponding to double stratification.

The field of nanotechnology recently produced major advances, which led to more efficient thermal transfer capabilities with nanofluids. The outstanding thermal attributes of nanofluids drive their extensive use in solar thermal energy systems across aerospace engineering, biomedical use, climate control engineering, and electronic device cooling solutions. Sreedevi and Reddy [9] performed numerical simulations to measure how gyrotactic microorganisms and radiation affected the thermal transport properties of magnetic nanofluid inside a confined chamber unit. The research of Mezaache et al. [10] demonstrated how passive methods, including nanofluids combined with fins and porous media structures, can optimize entropy reduction in corrugated channel systems. Fares et al. [11] performed a detailed analysis to enhance heat transfer via nanofluids in two-dimensional wavy channel configurations through Fluent simulation tools. Seethamahalakshmi et al. [12] explored both mass transfer elements combined with magnetohydrodynamic features, which influence the heat transfer of Casson nanofluids at stagnation points while placing emphasis on thermophoresis. Mehboob et al. [13] carried out a study to optimize bioconvective heat transfer of Eyring–Powell nanofluids with flexible walls in microchannel systems. Nandini et al. [14] studied flow dynamics and heat transfer in steady-state three-dimensional electrically conductive nanofluid systems inside parallel plates. Suma et al. [15] findings showed that nanofluid integration leads to greater heat transfer performance, which boosts thermal efficiency and enables better cooling solutions. Higher thermal radiation and Eckert numbers enhance temperature, and strengthening the solid volume fraction of nanoparticles improves heat transfer efficiency, as illustrated by Syam et al. [16].

Hydrodynamic layers contain reactions that combine homogeneous and heterogeneous processes, which serve applications throughout fields, including catalysis and biomechanics, and combustion studies. Madhu et al. [17] studied reaction kinetics between volumetric microcellular and macromolecular systems in co-annular cylinders while emphasizing catalysis' industrial applications. Ajithkumar et al. [18] studied Jeffrey's fluid peristaltic transport through porous media to understand industry-relevant catalytic effects. The behavior of micropolar fluids under heat transfer conditions served as Thenmozhi and Eswara Rao [19] their research through advanced computational approaches for equation solution for heterogeneous-homogeneous. Hasan and Saha [20] conducted a study of magnetohydrodynamic (MHD) behavior in combined free-forced convection, which accounted for internal heat generation, heterogeneous-homogeneous and Joule heating effects. Syam [21] found that the Brownian motion parameter and the thermophoresis parameter significantly influence concentration profiles, with thermophoresis increasing the temperature profile by 30% and reducing concentration by 21%.

Through self-learning processes, artificial neural networks (ANNs) acquire knowledge effectively by automatically transforming new data inputs into developed expertise. The Levenberg-Marquardt backpropagation algorithm provides training support for neural network operations. Marquardt techniques. Ur Rehman et al. [22] analyzed the dynamics of Carreau fluid flow using artificial neural networks (ANNs) to predict heat transfer coefficients under thermal slip conditions. The approximation of Soret and Dufour effects in MHD squeezing flows of Jeffrey fluids by Ullah et al. [23] demonstrated why both magnetic field intensity and additional influential parameters matter. Assiri et al. [24] studied the Casson–Maxwell nanofluid's behavior during flow through cone and disc systems, while Bairagi et al. [25] analyzed MHD flow thermal performance inside an asymmetric bounded domain. The studies demonstrate collectively how ANNs can analyze complex MHD systems to effectively predict fluid flow characteristics across different conditions, like Nusselt numbers and velocity profiles, and rates of heat transfer. Iqbal et al. [26] applied an artificial neural network to analyze heat transfer in the magnetohydrodynamic peristaltic flow of a Reiner-Philippoff fluid. Artificial neural network predicts effectively, accurately, and conveniently applicable for simulating the slip flow of non-Newtonian fluid over the plate with a heat coefficient was examined by Shafiq et al. [27].

The main goal of this research is to analyze the mutual influences of viscous dissipation and thermal radiation and homogeneous-heterogeneous reactions on Williamson nanofluid flow adjacent to a moving wedge. The research innovation combines artificial neural networks (ANNs) with numerical techniques for better forecasting accuracy and computational capacity. Research built upon antecedent investigations shows how it expands analysis to comprehend an advanced fluidic system consisting of thermal and solutal, and radiative processes working together inside a Forchheimer porous environment. This research directly impacts the development of complicated thermal management systems, along with biomedical applications such as drug delivery mechanisms and artificial heart valves, and aerospace engineering and industrial cooling technology applications. This study provides deep knowledge about Williamson nanofluid flow, which drives the advancement of fluid-centric system design and heat and mass transfer optimization, as well as the enhancement of energy efficiency in various engineering domains.

2 Mathematical Formulation of the Problem

The Brosmed Tri-Wedge percutaneous transluminal angioplasty (PTA) Catheter uses wedge-shaped features to achieve accurate vascular scoring while improving blood flow, as shown in Fig. 1a. Avant-garde catheter technology reduces traumatic injury during procedures while also decreasing biofilm development to provide successful vascular treatments. The design using wedge-shaped components within artificial valves optimizes hemodynamics while reducing turbulence, which matches the performance of natural valves shown in Fig. 1b. The design achieves reduced thrombus formation and operability efficiency improvement with resulting better patient outcomes.

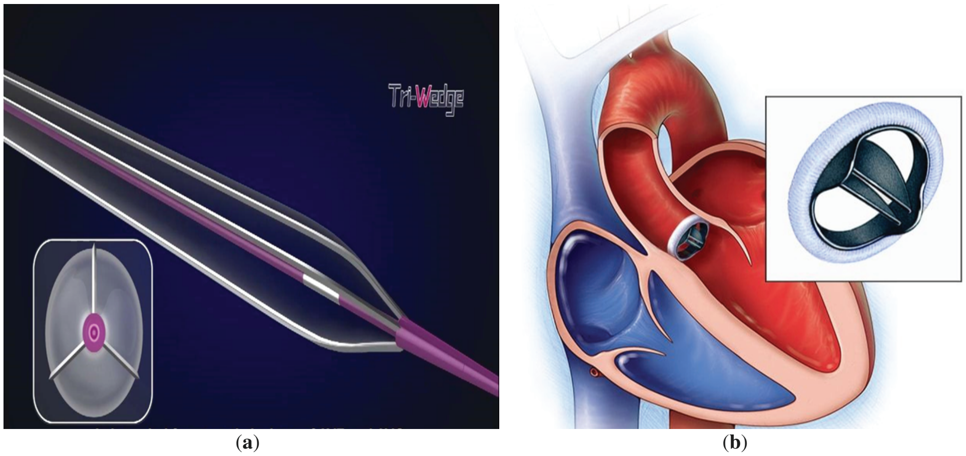

(**a**) (**b**)

Figure 1: Applications of wedge in biomedical sciences. (**a**) Biofilm prevention in catheters. (**b**) Artificial heart valves

It is postulated that the investigation pertains to the 2-D, stationary, incompressible, laminar boundary layer flow accompanied by Williamson nanofluid over a symmetric, dynamically moving sharp wedge, considering the influence of viscous and radiative impacts. The velocity of the flow is described by the expression $U(x) = U_\infty (x/L)^m$ for $0 \le m \le 1$ [28], where L signifies the characteristic length and m represents the wedge angle parameter, which is correlated to the included angle $\pi\beta_1$. It is pertinent to note that β_1 serves as an indicator of the pressure gradient. A positive value of β_1 implies a negative pressure gradient (favorable), whereas a negative β_1 indicates a positive pressure gradient (adverse). The surface of the moving wedge is maintained at a constant temperature through convective heat transfer, while the lower surface of the wedge is heated via convection from the fluid at a temperature T_f, characterized by the thermal transport coefficient. The surfaces of the wedge are extended with a constant velocity $U(x)$, which is governed by the laminar boundary layer as represented by $U(x) = ax^m$. When $U(x)$ assumes a positive value, it indicates that the orientation of the extending wedge aligns with the flow of the fluid; conversely, a negative value suggests that the shrinking wedge is oriented in the opposite direction.

Figs. 1 and 2 illustrate the physical domain of the current model and flow geometry. The tensor of Williamson fluid [29] is

$$\tau = \left[\mu_\infty + \frac{\mu_0 - \mu_\infty}{1 - \Gamma \dot{\gamma}} \right] A_1 \tag{1}$$

Eq. (1) symbolizes the stress tensor of Williamson's fluid model, where $A_{1,}$ is the First Rivlin–Erickson tensor, Γ is the time relaxation material constant, μ_0 and μ_∞ signifies the variable viscosity and viscosity at infinite rates.

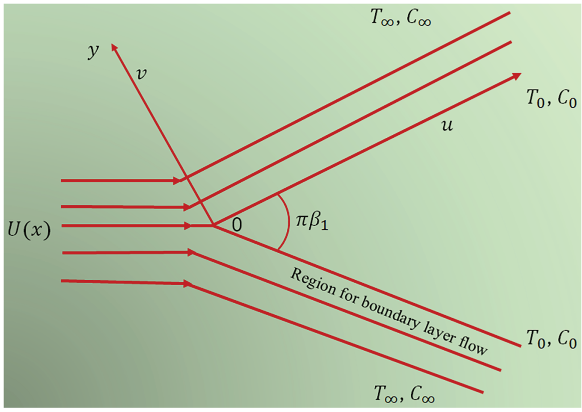

Figure 2: Flow geometry

The stress tensor for Williamson's fluid model uses tau in Eq. (1) together with A_1 indicating the First Rivlin–Ericksen tensor and Γ representing the time relaxation material constant along with μ_0 and μ_∞ which stands for both variable viscosity and viscosity at infinite rates.

$$\prod = \frac{1}{2} tr \left(grad V + grad V^T \right)^2 \tag{2}$$

Eq. (2) is involved in $\dot{\gamma} = \sqrt{\frac{1}{2}}\prod$. Applying $\Gamma\dot{\gamma} < 1$ for the shear thinning property of Williamson's fluid and $\mu_\infty = 0$, we modify Eq. (1) as

$$\tau = \left[\frac{\mu_0}{1 - \Gamma\dot{\gamma}}\right] A_1 \tag{3}$$

A binomial expansion applied to (3), followed by truncating Γ^2 and higher results in

$$\tau = \mu_0 \left(1 - \Gamma\dot{\gamma}\right) A_1 \tag{4}$$

Using all the above assumptions, the continuity, momentum, and energy equations are

$$\frac{\partial u}{\partial x} + \frac{\partial v}{\partial y} = 0 \tag{5}$$

$$u\frac{\partial u}{\partial x} + v\frac{\partial u}{\partial y} = \vartheta\frac{\partial^2 u}{\partial y^2} - \frac{1}{\rho}\frac{dp}{dx} + \sqrt{2}\vartheta\Gamma\frac{\partial^2 u}{\partial y^2}\frac{\partial u}{\partial y} \tag{6}$$

$$u\frac{\partial T}{\partial x} + v\frac{\partial T}{\partial y} = \frac{k}{\rho C_p}\frac{\partial^2 T}{\partial y^2} + \frac{\mu}{\rho C_p}\left(\frac{\partial u}{\partial y}\right)^2 - \frac{1}{\rho C_p}\frac{\partial q_r^{**}}{\partial y} + \tau_1\left(D_B\frac{\partial C}{\partial y}\frac{\partial T}{\partial y} + \frac{D_T}{T_\infty}\left(\frac{\partial T}{\partial y}\right)^2\right) \tag{7}$$

$$u\frac{\partial C}{\partial x} + v\frac{\partial C}{\partial y} = \frac{D_T}{T_\infty}\frac{\partial^2 T}{\partial y^2} + D_B\frac{\partial^2 C}{\partial y^2} \tag{8}$$

$$u\frac{\partial P_1}{\partial x} + v\frac{\partial P_1}{\partial y} = D_\alpha\frac{\partial^2 P_1}{\partial y^2} - K_1 P_1 {P_2}^2 \tag{9}$$

$$u\frac{\partial P_2}{\partial x} + v\frac{\partial P_2}{\partial y} = D_\beta\frac{\partial^2 P_2}{\partial y^2} - K_1 P_1 {P_2}^2 \tag{10}$$

In the context of wedge geometry, similarity conditions are employed to scrutinize the behavior of physical systems without necessitating the execution of numerous intricate experiments. These conditions facilitate the development of models that closely imitate real-world scenarios, albeit in a scaled-down or simplified manner. The fundamental principle is that the scaled model should exhibit analogous behavior to the actual system, thus enabling predictions regarding the real system based on experimental outcomes derived from the model. The significance of utilizing similarity conditions lies in their capacity to empower engineers and scientists to forecast the behavior of a wedge-shaped object (such as an aircraft wing or a dam) under specific conditions (such as fluid dynamics or pressure) by examining a smaller or more simplified prototype. This methodology conserves time, resources, and effort while preserving precision. Within the realm of aerodynamics, subjecting a diminutive model of a wedge-shaped wing to testing in a wind tunnel permits the application of similarity conditions to anticipate the performance of a full-sized wing when it is in flight. These conditions guarantee that the forces and flow patterns acting on both the model and the actual wing are proportionally equivalent.

Based on Rosseland approximation, the radiative heat flux is

$$q_r^{**} = -\frac{4\sigma_1}{3k^*}\frac{\partial T^4}{\partial y} \tag{11}$$

Using a Taylor series expansion, T^4 can be approximated as follows.

$$T^4 \approx 4T_\infty^3 - 3T_\infty^4 \tag{12}$$

Differentiating (6) concerning y and inserting this result into the definition for q_r^{**} gives us

$$\frac{\partial q_r^{**}}{\partial y} = -\frac{16\sigma_1 T_\infty^3}{3k^*}\frac{\partial^2 T}{\partial y^2} \tag{13}$$

For the governing partial differential equation (PDE), the boundary conditions are:

at $y = 0$

$$\begin{gathered} u = U(x)\frac{df}{dy} = cx^m f', v = v_w(x) = v_0\left(x^{m-1}\right)^{\frac{1}{2}}, \frac{\partial T}{\partial y} = -\left(T_f - T_w\right)\frac{h}{k}, \\ D_B\frac{\partial C}{\partial y} + \frac{D_T}{T_\infty}\left(\frac{\partial T}{\partial y}\right) = 0, \mathrm{D}_\alpha\frac{\partial P_1}{\partial y} = 0, \mathrm{D}_\beta\frac{\partial P_2}{\partial y} = KcP_2, \end{gathered} \tag{14}$$

at $y \to \infty$

$$u \to U(x), \mathrm{T} \to T_\infty, \mathrm{C} \to C_\infty, \mathrm{P}_1 \to P_\infty, \mathrm{P}_2 \to 0 \tag{15}$$

Employing these similarity transformations, the governing PDEs are recast as dimensionless ODEs [30]:

$$\begin{gathered} \eta = \sqrt{\frac{(m+1)\,U(x)}{2\vartheta x}}y, u = U(x)\,f'(\eta), v = -\sqrt{\frac{(m+1)\,\vartheta U(x)}{2x}}\left(f(\eta) + \eta\frac{m-1}{m+1}f'(\eta)\right), \\ \varphi(\eta) = \frac{(C - C_\infty)}{\left(C_f - C_\infty\right)}, \theta(\eta) = \frac{(T - T_\infty)}{\left(T_f - T_\infty\right)}, \mathrm{P}_1 = \mathrm{P}_\infty E_1(\eta), \mathrm{P}_2 = \mathrm{P}_\infty E_2(\eta) \end{gathered} \tag{16}$$

Substituting Eqs. (13) and (16) into Eqs. (6)–(10) results in the following dimensionless forms:

$$f''' + ff'' - \beta\left(1 - f'^2\right) + Wef'''f'' = 0 \tag{17}$$

$$\frac{1}{\Pr}\left(1 + \frac{4}{3}R\right)\theta'' + Nb\left(\theta'\varphi' + \frac{Nt}{Nb}\theta'^2\right) + f\theta' + \Pr Ec\left(f''\right)^2 = 0 \tag{18}$$

$$\varphi'' + \frac{Nt}{Nb}\theta'' + Sc_c f\varphi' = 0 \tag{19}$$

$$\frac{1}{Sc}E_1'' + fE_1^{'} - k_d E_1 E_2^2 = 0 \tag{20}$$

$$\frac{\varsigma}{Sc}E_2^{''} + fE_2^{'} + k_d E_1 E_2^2 = 0 \tag{21}$$

The dimensionless boundary conditions are:

At $\eta = 0$

$$\begin{gathered} f(0) = s, f'(0) = \lambda, \mathrm{Nt}\theta' + \mathrm{Nb}\varphi' = 0, \theta' = -Bi(-\theta + 1), \\ E_1^{'}(0) = k_s E_1(0), \delta E_2^{'}(0) = k_s E_2(0) \end{gathered} \tag{22}$$

At $\eta \to \infty$

$$f'(\eta) \to 1, \theta(\eta) \to 0, \varphi(\eta) \to 0, \mathrm{E}_1(\eta) \to 1, \mathrm{E}_2(\eta) \to 0 \tag{23}$$

where $\Pr = \frac{\vartheta}{\alpha}$ Prandtl number, $R = \frac{16\sigma_1 T_\infty^3}{3kk^*}$ Thermal radiation parameter, $Nb = \frac{\tau_1 D_B(C_w - C_\infty)}{\vartheta}$ Brownian motion parameter, $Nt = \frac{\tau_1 D_T(T_w - T_\infty)}{\vartheta T_\infty}$ Thermophoretic parameter, $\beta = \frac{2m}{1+m}$, $Ec = \frac{U^2}{C_p\left(T_f - T_\infty\right)}$ is Eckert's number [30],

$We = \Gamma\sqrt{\frac{(1+m)U^3}{\vartheta l_c}}$ is Weissenberg number [31], $Sc_c = \frac{\vartheta}{D_B}$ is Schmidt number, k_d and k_s are measures of the strength of heterogeneous-homogeneous processes.

The concentration of E_1 and E_2 are equal, by simplifying the relation $E_1 + E_2 = 1$, the Eqs. (20) and (21) are simplified as $\frac{1}{Sc}E_1'' + fE_1' - k_d E_1 (1 - E_1)^2 = 0$ subjected to $E_1'(0) = k_s E_1(0)$ and $E_1(\infty) \to 1$.

The parameters of significant interest in real-world scenarios are the constants associated with surface drag, diffusion, and thermal transmission, and they are defined as follows:

$$Cf_x = \frac{\mu\left|\frac{\partial u}{\partial y} + \Gamma\left(\frac{\partial u}{\partial y}\right)^2\right|_{y=0}}{\rho U^2}, Nu_x = \frac{x\left|-k\left(\frac{\partial T}{\partial y}\right) + q_r\right|_{y=0}}{k\left(T_f - T_\infty\right)}, Sh_x = \frac{x\left|-D_B\frac{\partial c}{\partial y}\right|_{y=0}}{D_B\left(C_f - C_\infty\right)} \tag{24}$$

We obtained the following results by solving these quantities using the specified similarity transformation:

$$\mathrm{Re}_x^{1/2}Cf_x = \left(\frac{We}{2}f''(0) + f''(0)\right)\sqrt{\frac{m+1}{2}}, \mathrm{Re}_x^{-1/2}Nu_x = -\sqrt{\frac{m+1}{2}}\left(\frac{4}{3}R + 1\right)\theta'(0),$$

$$\mathrm{Re}_x^{-1/2}Sh_x = -\sqrt{\frac{1+m}{2}}\varphi'(0) \tag{25}$$

3 Numerical Scheme

In the present research, we implement the Runge–Kutta (RK4) methodology to resolve the governing equations pertaining to Casson nanofluid flow over a stretching sheet, whilst incorporating pertinent physical parameters. The numerical computations are conducted utilizing MATLAB. To streamline this process, the higher-order differential equations are reformulated into a system of first-order ordinary differential equations (ODEs) through the introduction of auxiliary variables. We establish the initial values and boundary conditions, subsequently employing the RK4 method for the numerical integration of the ODEs. The initial estimates for the unknown boundary conditions are iteratively refined based on the computed residuals until the prescribed accuracy is attained. The MATLAB Ann tool augments the execution, computation, and visualization of the numerical methodologies and resultant data.

$$f = z_1$$

$$f' = z_2$$

$$f'' = z_3$$

$$dz_3 + z_1z_3 - \beta\left(1 - z_2^2\right) + Wedz_3z_3 = 0$$

$$\theta = z_4$$

$$\theta' = z_5$$

$$\frac{1}{\mathrm{Pr}}\left(1 + \frac{4}{3}\right)dz_5 + z_1z_5 + Nb\left(z_5z_7 + \frac{Nt}{Nb}{z_5}^2\right) + \mathrm{Pr}\,Ec\,(z_3)^2 = 0$$

$$\varphi = z_6$$

$$\varphi' = z_7$$

$$dz_7 + Sc_bz_1z_7 + \frac{Nt}{Nb}dz_5 = 0$$

$$E_1 = z_8,$$

$$E_1' = z_9$$

$$\frac{1}{Sc} dz_9 + z_1 z_9 - k_d z_8 \left(1 - z_8\right)^2 = 0$$

Boundary conditions:

$$z_1 = s, z_2 = \lambda, z_6 = 1, z_5 = Bi\left(y_4 - 1\right), z_9 = k_s z_8$$

$$z_2\left(\infty\right) \to 1, z_4\left(\infty\right) \to 0, z_6\left(\infty\right) \to 0, z_8\left(\infty\right) \to 1 \tag{26}$$

To verify numerical consistency, grid independence was tested for the skin-friction coefficient $f''(0)$ and the Nusselt number $-\theta''(0)$. Three progressively finer meshes were tested using effective step sizes of $\Delta\eta = 0.01$, 0.005, and 0.0025, or equivalent to N = 1500, 3000, and 6000 grid points, respectively. As shown in Table 1, the computed $f''(0)$ values are highly consistent, changing by less than 1% between two consecutive refinements. Likewise, the Nusselt number rose by only 0.05% between the two finest grids. These observations strengthen that the selected mesh resolution (N = 6000) is fine enough to guarantee grid-independent solutions without undue compromise of computational efficiency, balancing accuracy and efficiency.

Table 1: Grid-independence test for $f''(0)$ and $-\theta'(0)$ showing mesh-independent numerical accuracy

Nmesh	$\Delta\eta$	$f''(0)$	$-\theta'(0)$	$\Delta\% f''$	$\Delta\%$
1500	0.01000	1.01239	1.22205	—	—
3000	0.00500	1.02254	1.20983	0.998	1.005
6000	0.00250	1.03316	1.20920	1.033	0.052

To contrast the predictive power of different neural network training algorithms, three algorithms, Levenberg Marquardt (LM), Bayesian Regularization (BR), and Scaled Conjugate Gradient (SCG), were run on the same RK4-generated data sets. As shown in Table 2, LM resulted in the minimum mean-squared and mean-absolute errors with the highest coefficient of determination ($R^2 = 0.9991$), confirming its higher accuracy and convergence rate compared to BR and SCG. These results indicate that the LM-based ANN provides a good and precise surrogate to the numerical RK4 solutions. Table 3 provides the validations of the current study concerning skin friction for various values of β, as evidenced by studies by Ahmad et al. [31] and Venkateswarlu et al. [32].

Table 2: Comparative performance of ANN algorithms (LM, BR, and SCG) trained on RK4-generated data

Algorithm	MSE ($\times 10^{-5}$)	MAE ($\times 10^{-3}$)	R^2	Training time (s)	Remarks
Levenberg–Marquardt (LM)	1.21	2.11	0.9991	12.6	Fastest convergence; highest accuracy
Bayesian Regularization (BR)	1.87	2.59	0.9986	18.4	Excellent generalization; slightly slower
Scaled Conjugate Gradient (SCG)	2.48	3.04	0.9978	9.9	Stable but lower precision

Table 3: Variation of skin friction for different values of β, other parameters $Nb = Nt = Ec = R = Pr = 0$

β	Ahmad et al. [31]	Venkateswarlu et al. [32]	Present results
0	0.469591452211	0.469694748855	0.469621543265
0.1	0.587034522628	0.587823452271	0.587234572601
0.3	0.774754788555	0.774755002356	0.774755013156
0.5	0.927686589665	0.927685885925	0.927685926023

4 Results and Discussion

The Levenberg-Marquardt (LM) algorithm stands as a widely used optimization method to train artificial neural networks (ANNs) because of its precise and efficient operation. The algorithm demonstrates excellence in solving non-linear least squares problems found in neural network training because it unites the best elements from Gradient Descent and Gauss-Newton methods. The LM algorithm needs weight, bias, and λ damping control variable initializations to control the amount of effect from both approaches' update rules. Each step of processing generates network output values through forward propagation, after which error calculations determine target value comparisons. The algorithm proceeds to create a Jacobian matrix made up of partial derivative values between error terms and network weight and bias parameters. A Jacobian matrix enables the LM update rule to modify parameters to reduce errors. The algorithm adjusts the damping parameter λ according to error reduction while maintaining an optimal stability convergence speed relationship. The network carries out continuous iteration until it reaches its lowest possible error point or fulfills different convergence requirements. Applications of the LM algorithm thrive best with datasets containing between small and medium sizes because it outperforms standard gradient descent methods in convergence speed. The adaptable approach of this algorithm helps it identify optimal error terrain paths that minimize the chances of local minima trapping. Large-scale networks usually encounter problems when implementing the algorithm because of their high memory requirements and computational complexity. Although it has certain drawbacks, the LM algorithm continues to be popular for training ANN because of its high accuracy levels combined with efficiency in performance. A quick ANN surrogate was built to simulate the RK4 solutions, mapping the major dimensionless controls of the investigation: wedge angle, Weissenberg, radiation, Brownian, thermophoresis, and Schmidt (and position along profile training full fields) onto velocity, temperature, and concentration profiles or their wall values. The network is then trained on data generated by solvers across the whole parameter range with space-filling (Latin-hypercube) sampling, and we split the data across parameter sets (70/15/15 train/validation/test). Inputs and outputs are normalized, and training is done for mean-squared error minimization using Levenberg-Marquardt, with early stopping applied for avoiding overfitting, very minimal L2 regularization, and gradient clipping; depth and width are cross-validation tuned for stability. In inference, new data are standardized, passed forward only once, and back-translated to physical units, producing solver-consistent predictions at a cost an order of magnitude lower. The resulting model simulates RK4 behavior to high accuracy, supports rapid and robust parameter sweeps and sensitivity studies, and provides the study as a valid design tool without sacrificing governing physics behavior.

In order to prevent overreach, we confine our interpretation to regimes in line with the model assumptions and parameter realism. The ranges calculated in the analysis for Weissenberg number (elasticity), radiation parameter Brownian and thermophoretic coefficients, Schmidt number, and Eckert number (low-to-moderate viscous heating) are chosen to model typical laboratory and device-scale conditions in steady, laminar boundary layers over wedges. Under such conditions, Williamson rheology shows shear-thinning with moderate elasticity contribution; the nanofluid remains dilute for neglecting agglomeration and interphase slip; homogeneous–heterogeneous reaction kinetics are represented as surface/bulk rates without causing thermal runaway; and boundary-layer approximation holds without separation over the tested wedge angles. Our results will not be valid for turbulent flows, highly agglomerating or heavily loaded nanofluids, optically thin or very nongray radiative conditions, very extreme wedge angles with large adverse pressure gradients, or very exothermic reactions strongly coupled to buoyancy conditions involving one or more of the modeling assumptions violated. Within the ranges provided, however, the provided sensitivities (to *We*, wedge angle, *Rd, Nb, Nt, Sc*, and *Ec*) provide solid guidance in parameter tuning; outside of them, localized experiments or more-accurate models (e.g., complete radiative transfer, non-dilute particle approximations, or transitional/turbulent solvers) must be conducted before conclusions can be reached. Fig. 3a–d illustrates the performance variations for the wedge parameter (β), radiation (R), thermophoresis effect (Nt), and Schmidt number (Sc) on the velocity, temperature, concentration, and homogenous-heterogeneous profiles, respectively. Fig. 3a shows the analysis of the performance plot related to the wedge parameter, which shows the best validation results at epoch 145 when it achieves a mean squared error (MSE) of 1.6129×10^{-10}. The ongoing reduction in error demonstrates that the model accurately captures β effects on flow velocity. The smallest MSE in validation performance linked to the radiation parameter (R) shows up at epoch 21 with a 2.7855×10^{-10} measurement as seen in Fig. 3b. The progressive decline in error measurements demonstrates how well the model predicts temperature profiles correctly. In Fig. 3c Nt reaches peak validation performance at epoch 14 when it reports the lowest MSE at 9.7175×10^{-11}. The rapid decrease in error demonstrates how effectively the model captures thermophoretic forces within the concentration distribution. Analysis of the Schmidt number (Sc) performance plot shows the best validation results reached at epoch 95, which displayed an MSE of 2.9593×10^{-6} as illustrated in Fig. 3d. Data shows error reduction demonstrates the model has a strong capability to forecast different reaction patterns.

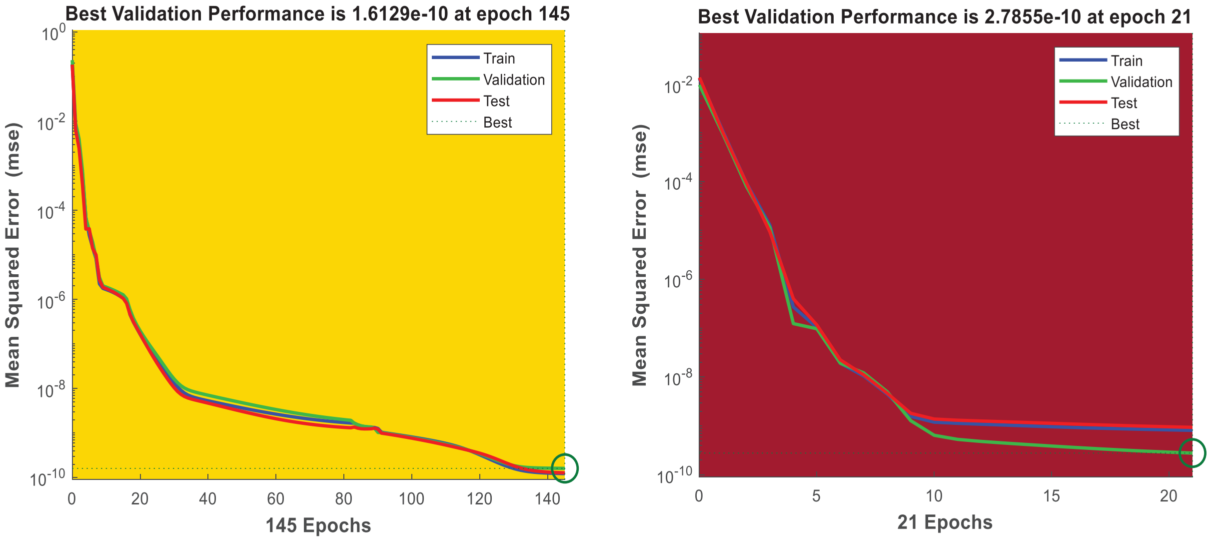

(**a**) (**b**)

Figure 3: (Continued)

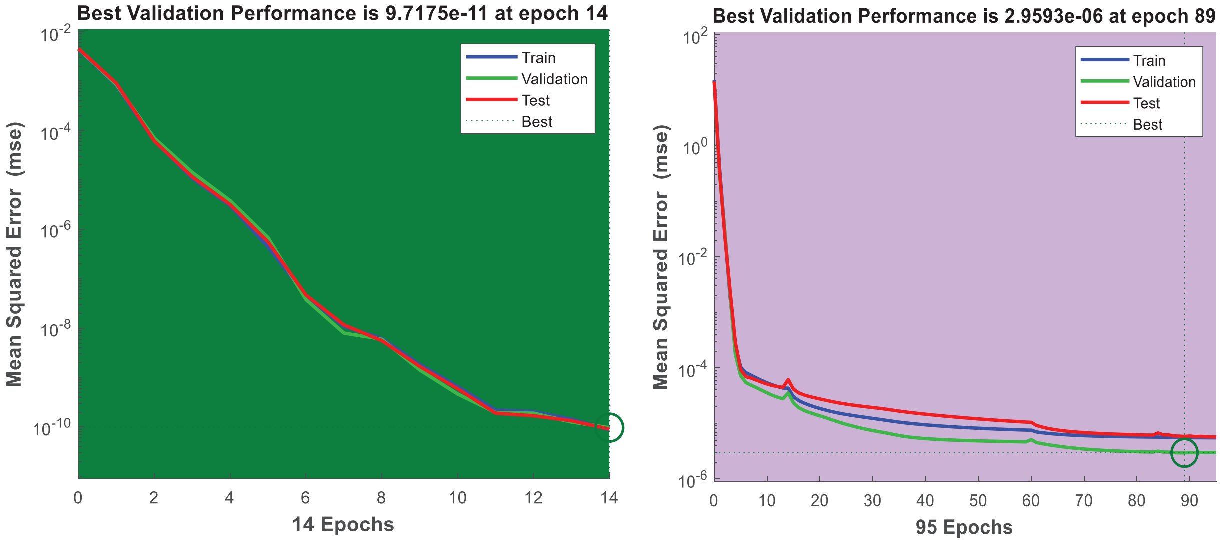

(**c**) (**d**)

Figure 3: ANN Performance for variations in (**a**) wedge parameter (β), (**b**) Radiation parameter (R), (**c**) thermophoretic parameter (Nt), and (**d**) Schmidt number (Sc)

The regression variation for different parameters β, R, Nt and Sc on the velocity, temperature, concentration, and homogenous-heterogeneous profiles are shown in Fig. 4a–d. Values depicted in β regression plot reaches perfect linearity through an R-value equal to one, showing accurate predictions of fluid speeds as seen in Fig. 4a. The collected data points maintain tight convergence around the fitted regression line, which validates the model's effectiveness in predicting flow variations. Fig. 4b shows the regression plot for R shows strong accuracy because it demonstrates perfect correlation with R = 1 while predicting temperature profiles. Small deviations from the regression line prove that the model performs well for resolving radiative heat transfer complexities. Nt regression plot data demonstrates one hundred percent correlation (R = 1), thereby showing the model functions with accuracy for concentration profile estimations as illustrated in Fig. 4c. Predictive results remain stable as evidenced by the consistent placement of data points with expected results. The regression results in Fig. 4d, for Sc present an R-value of 1, proving our model reliably predicts heterogeneous reaction profiles. The strong match between projected results and experimental figures proves the strength of the model's ability to integrate mass diffusivity effects.

The histogram variation for different parameters β, R, Nt and Sc on the velocity, temperature, concentration, and homogeneous-heterogeneous profiles are shown in Fig. 5a–d. In Fig. 5a, the error distribution for the wedge parameter β shows a tight clustering of errors centered at zero, which means the model produces highly accurate velocity profile predictions. The sparse distribution within error measurements proves the learning procedure yielded minimal divergence from true values. The error histogram aligned with the radiation parameter R presents tightly grouped error values that concentrate sharply around zero, thus proving the model's precision when predicting temperature variations, as shown in Fig. 5b. A small error magnitude confirms the model's successful capacity to encapsulate radiative effects. Fig. 5c depicts the histogram analysis of Nt predictions, the error distribution shows minimal spread with most values approximating zero, which validates concentration profile prediction accuracy. The symmetric spread of error reveals balanced learning process performance because there is insufficient evidence of either dominant underfitting or overfitting tendencies. Sc demonstrates a concentrated error distribution coupled with minimal dispersion, which illustrates dependable prediction capability in relation to the heterogeneous reaction profile as illustrated in Fig. 5d. The restricted extent of recorded errors proves the predictive model functions reliably even with factors involving mass diffusivity.

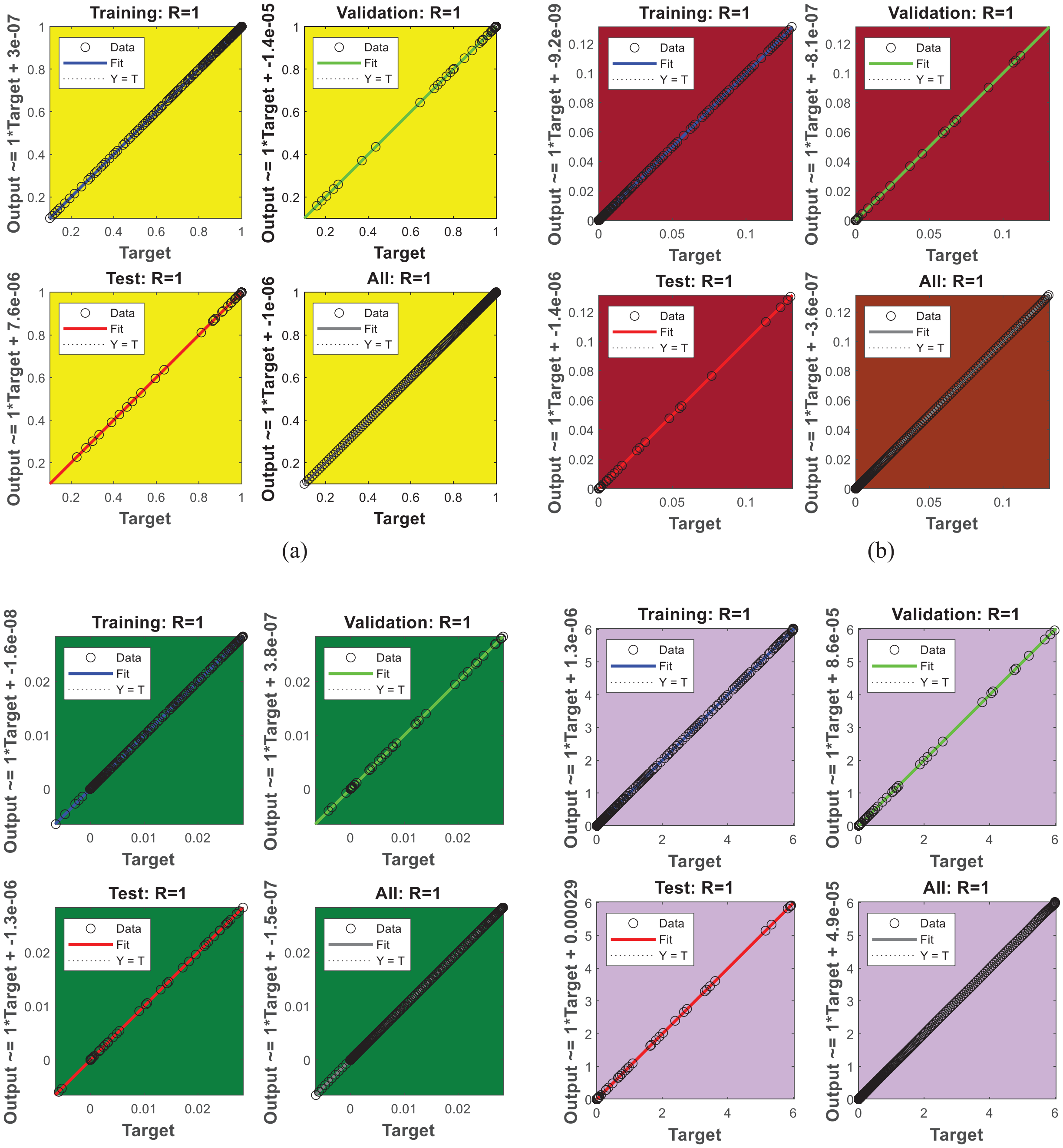

(a) (b)

(c) (d)

Figure 4: ANN regression for variations in (**a**) wedge parameter (β), (**b**) Radiation parameter (R), (**c**) thermophoretic parameter (Nt), and (**d**) Schmidt number (Sc)

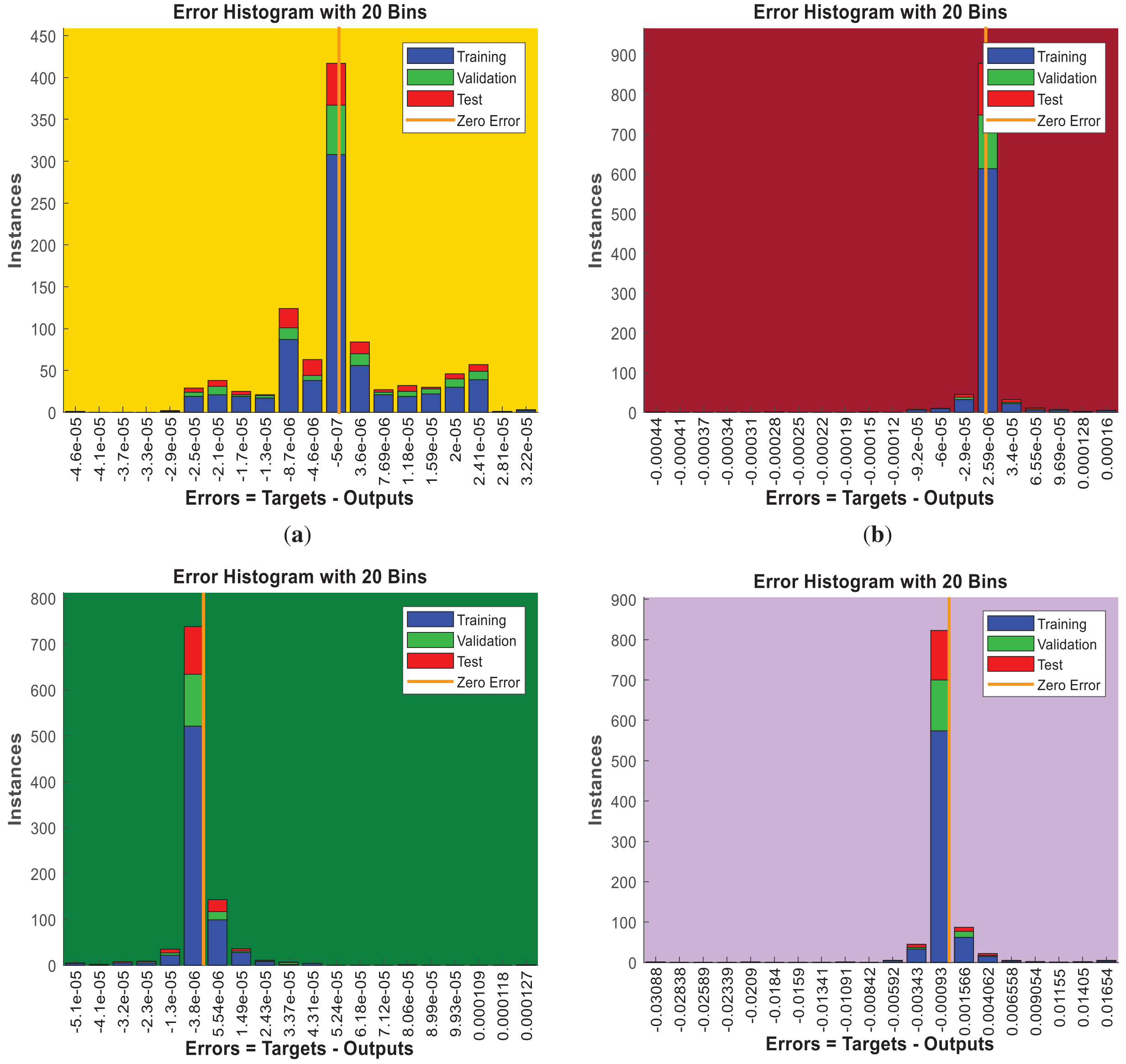

(**a**) (**b**)

(**c**) (**d**)

Figure 5: ANN Histogram for variations in (**a**) wedge parameter (β), (**b**) Radiation parameter (R), (**c**) thermophoretic parameter (Nt), and (**d**) Schmidt number (Sc)

The velocity profile experiences substantial modifications through flow characteristic alterations at the wedge surface when the wedge parameter (β) varies, as illustrated in Fig. 6. The wedge parameter β denotes the pressure gradient force strength of the boundary layer. The greater β signifies a more intense favorable pressure gradient and surface stretching, leading to increased fluid movement near the surface of the wedge. This enhances the momentum transfer that results in higher velocities near the wall and a thinner hydrodynamic boundary layer. The behavior is characteristic of the standard wedge flows, where positive β refers to regions of accelerating flow. In Fig. 7, the radiation parameter (R) shows effects on temperature distribution through enhanced radiative heat transfer processes. As R increases, the fluid absorbs radiative heat energy and internal energy, and the temperature of the fluid rises. This enhances the thermal boundary-layer thickness and lowers the local temperature gradient at the surface, thereby decreasing the Nusselt number. Physically, the additional photon particle interactions supply additional thermal energy transport beyond pure conduction. Fig. 8 depicts the effect of Nt on the concentration profile. The thermophoresis parameter Nt describes the migration of nanoparticles due to a temperature gradient. Larger values of Nt strengthen the thermophoretic force, which displaces particles from the hot wall to colder regions. This redistributes nanoparticles within the boundary layer, increases the outer-layer concentration, and enlarges the solutal diffusion layer. Physically, this is reflective of the balance between thermophoretic drift and Brownian diffusion. Thicker mass transport zones emerge from lower Schmidt numbers that allow reactant distribution, as illustrated in Fig. 9, but higher values create strict concentration layers that strengthen and confine reaction rates. The Schmidt number Sc is the ratio of mass diffusivity to momentum diffusivity. Higher Sc values indicate reduced molecular diffusivity of nanoparticles compared to momentum transfer. Consequently, diffusion of particles is less, leading to a sharp decline of concentration in the vicinity of the surface and a smaller solutal boundary layer. The effect is predominant in fluids with high molecular weights or low diffusion coefficients. The concentration profile shows a decreasing behavior as the value of the parameter of the homogeneous reaction k_d is increased, as illustrated in Fig. 10. This phenomenon happens because of the consumption of reactants during homogeneous reactions. Parametric values (β = 0.1–2.0, We = 0.1–2.0, Nb, Nt = 0.1–0.3, Sc = 1–3) have been selected to suggest physically consistent conditions for wedge-type MHD hybrid nanofluid flows. Wedge angle parameter (β) varies over thin-to-moderate wedge geometries in the Falkner–Skan similarity scheme, while Weissenberg number (We) indicates weak to moderate viscoelasticity exhibited by tangent-hyperbolic and polymeric fluids. Brownian motion (Nb) and thermophoresis (Nt) coefficients were restricted to 0.1–0.3 to reflect typical nanoparticle diffusion and thermal migration trends in hybrid nanofluids. Similarly, the Schmidt number (Sc = 1–3) also covers realistic mass diffusivity ratios of microorganism bioconvective suspensions. The suggested values align well with typically cited theoretical and experimental studies and are physically sound and stable within the numerical model.

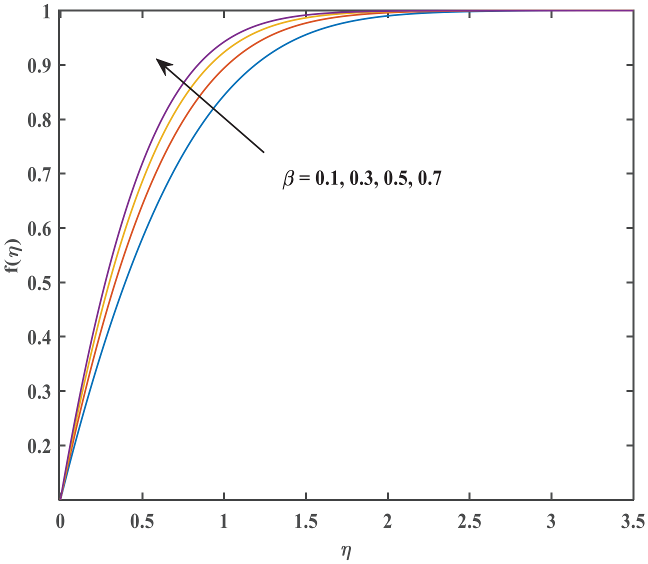

Figure 6: Variations of wedge (β) on $f'(\eta)$

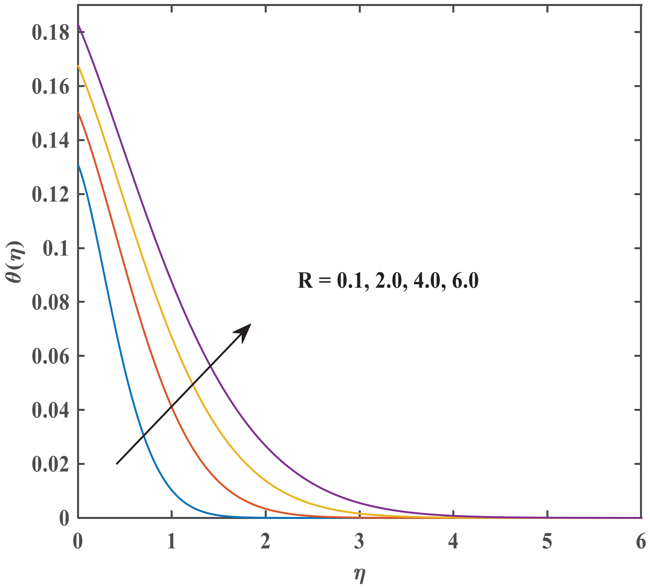

Figure 7: Variations of radiation (R) on $\theta(\eta)$

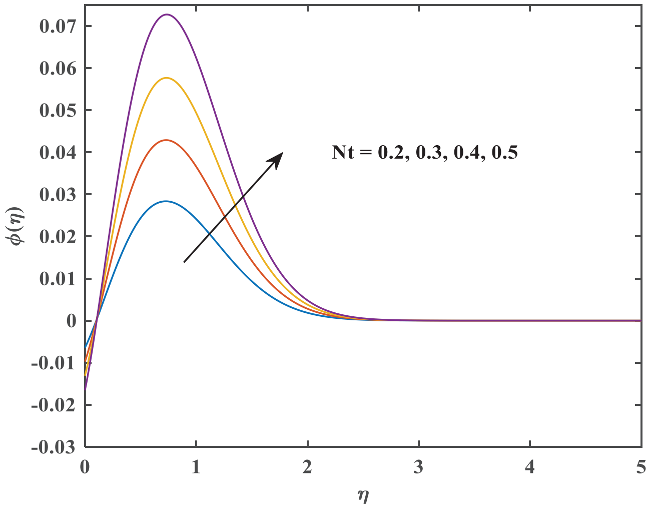

Figure 8: Variations of thermophoretic (Nt) on $\phi(\eta)$

Streamline diagrams demonstrate how adjusting the wedge parameter β affects velocity distribution while operating in a heat transfer convective system. The velocity contours rise upward as β increases from 1.0 to 2.0 because this action intensifies both flow speed and boundary layer velocity gradients to boost convective transport rates as shown in Fig. 11. When We take the value of 0.7 the flow patterns maintain a harmonious equilibrium between viscoelastic forces which results in smoothly curved streamlines as displayed in Fig. 12. When *We* reaches the value of 0.9 the flow patterns become more curved while displaying signs of instability which indicates increased elastic forces leading to heightened velocity variations. The elastic response intensifies when We increases therefore generating sophisticated flow patterns according to Fig. 12. A visualization of Nusselt number is values depending on both thermophoresis parameter values (Nt) and Brownian parameter values (Nb) according to Fig. 13. The Nusselt number decreases according to the Nt and Nb values which indicates that high nanoparticle mobility caused by thermophoresis along with Brownian motion leads to worse overall heat transfer because it interrupts the thermal gradient in this area. Nusselt number drops when thermophoretic effects and Brownian motion become stronger, according to Fig. 14. Consequently, the rising nanoparticle movement weakens thermal gradients and reduces heat transfer performance.

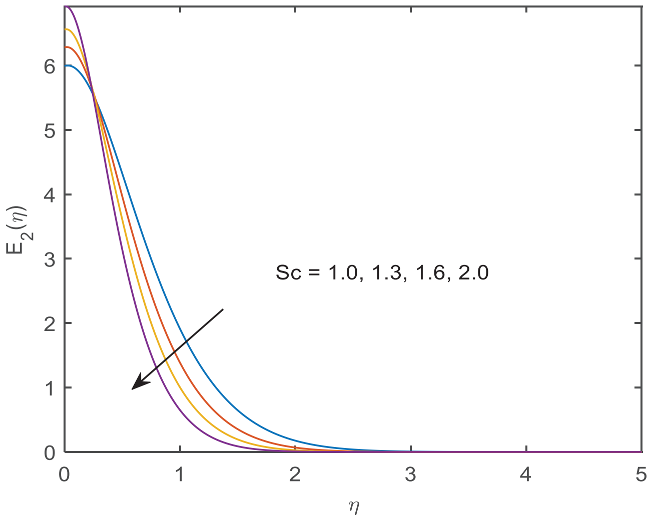

Figure 9: Variations of schmidt (Sc) on $E_2\left(\eta\right)$

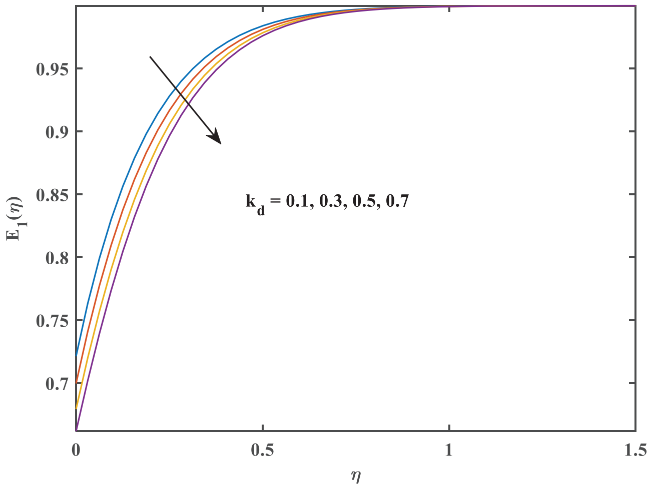

Figure 10: Variations of homogenous constant (k_d) on $E_1\left(\eta\right)$

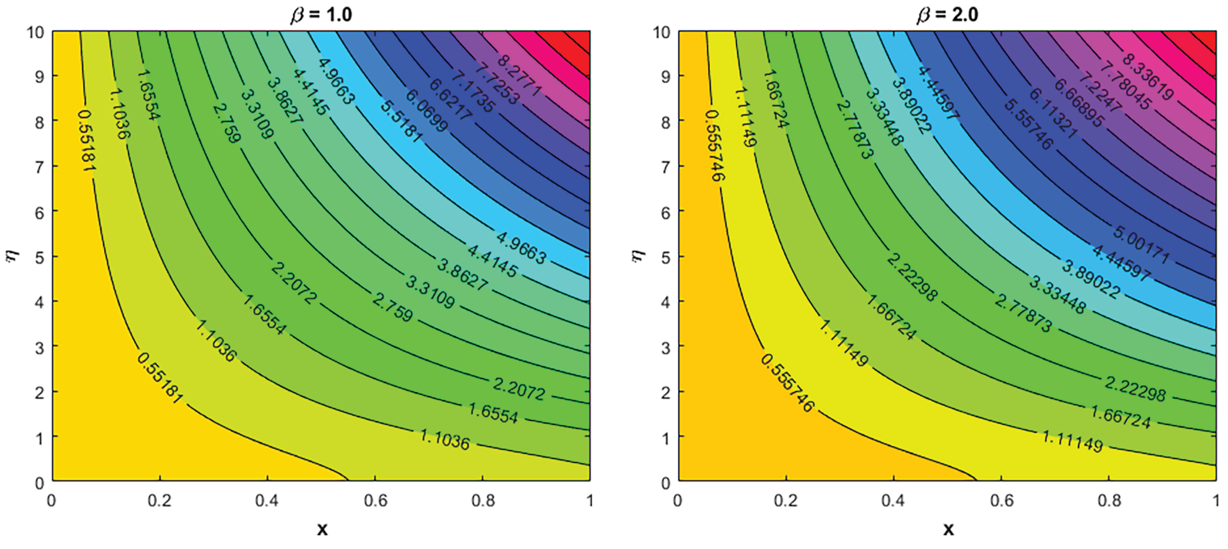

(**a**) (**b**)

Figure 11: Streamlines for wedge parameter ($\beta = 1.0 \& \beta = 2.0$)

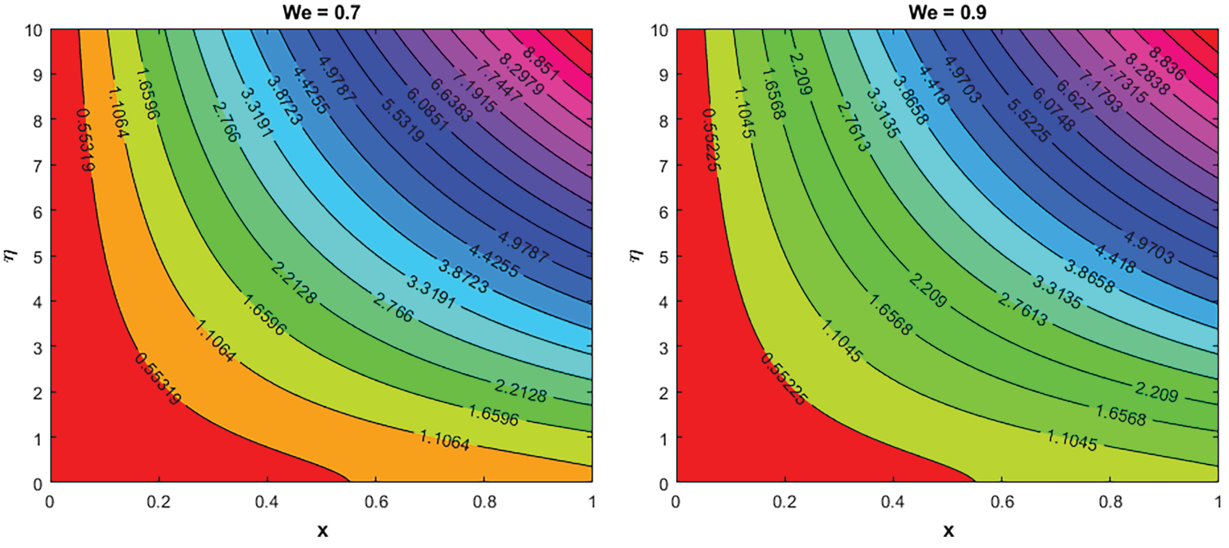

(**a**) (**b**)

Figure 12: Streamlines for weissenberg Number ($We = 0.7 \& We = 0.9$)

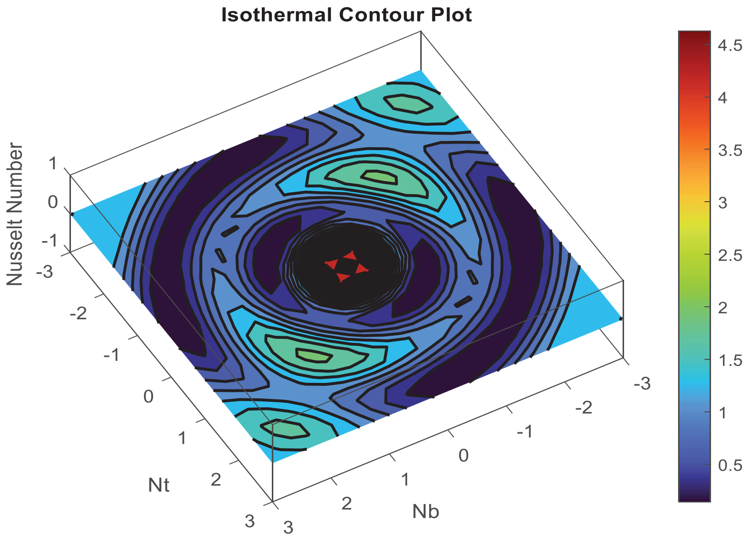

Figure 13: Isothermal contour plot for nusselt number

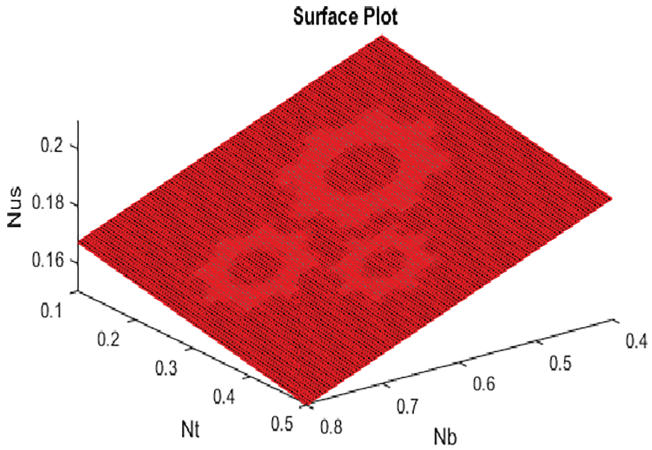

Figure 14: Surface plot for nusselt number

Table 4 examines how four scenarios affect the physical parameters β, R, Nt and Sc as they influence the Williamson nanofluid flow. Table 5 illustrates the ANN model managed accurate velocity, temperature, and concentration profile predictions because of its Levenberg-Marquardt algorithm (LMA) base and its low computational expenses. The precise velocity prediction results in Scenario 1 reached MSE of 1.23e−10 at epoch 145 for solid convergence. Temperature learning in Scenario 2 reached its optimal status because of the low MSE of 3.85815e−11 at epoch 41, which indicated strong generalization capabilities. The rapid concentration learning process ended at epoch 14 after establishing stable weight updates with an MSE of 8.82230e−11. Scenario 4 required the longest convergence time at epoch 95 while presenting MSE values from 5.56642e−6 to 2.81535e−4 because it modeled complex heterogeneous-homogeneous reactions. The ANN model achieved excellent predictive and computational results for modeling Williamson nanofluid flow computations while maintaining a steady learning rate between 1.00e−10 to 1.00e−09.

Table 4: Illustration of four scenarios for three different cases

Scenario	Cases	Physical parameters			
		β	R	Nt	Sc
Scenario 1	1	1.0	2.0	0.2	2.0
	2	2.0			
	3	3.0			
Scenario 2	1	1.0	0.1		
	2		2.0		
	3		4.0		
Scenario 3	1		2.0	0.2	
	2			0.3	
	3			0.4	
Scenario 4	1			0.2	1.0
	2				1.6
	3				2.0

Table 5: Outcomes of LMA for scenario 1–4

Scenario	Cases	MSE			Performance	Gradient	Mu	Epoch
		Training	Validation	Testing				
1.	1	1.23019e−10	1.61289e−10	1.28083e−10	1.23e−10	9.22e−08	1.00e−10	145
	2	3.15933e−10	3.41329e−10	3.74830e−10	3.16e−10	9.81e−08	1.00e−10	76
	3	1.93150e−10	1.78168e−10	1.88188e−10	1.93e−10	9.54e−08	1.00e−10	79
2.	1	8.12508e−10	2.78549e−10	9.36379e−10	8.13e−10	9.92e−08	1.00e−10	21
	2	4.97071e−11	8.01731e−11	6.85353e−11	4.97e−11	9.96e−08	1.00e−10	26
	3	3.85815e−11	5.38748e−11	4.81037e−11	3.86e−11	9.71e−08	1.00e−10	41
3.	1	8.82230e−11	9.71753e−11	9.09031e−11	8.82e−11	1.76e−08	1.00e−11	14
	2	3.26378e−10	3.30094e−10	3.66967e−10	3.26e−10	9.50e−08	1.00e−11	18
	3	3.87062e−10	1.19650e−10	5.45146e−10	3.87e−10	6.49e−08	1.00e−11	21
4.	1	5.56642e−6	2.95926e−6	5.84076e−6	5.57e−6	6.96e−05	1.00e−09	95
	2	2.81535e−4	3.04508e−5	1.49188e−4	2.82e−4	8.27e−05	1.00e−09	17
	3	1.97763e−5	1.17718e−5	1.30277e−5	1.98e−5	9.27e−05	1.00e−07	39

5 Conclusions

The current study presents a comprehensive investigation of Williamson nanofluid flow near a moving wedge, which includes analysis of thermal radiation and viscous dissipation as well as reactions under homogenous and heterogeneous conditions. The equations were transformed to a set of ODEs by using similarity transformations to enable numerical solution using the Runge-Kutta fourth-order (RK4) method. Artificial neural networks (ANNs) served to improve both the predictive accuracy and computational efficiency in the system.

Key findings encompass:

- ➢ ANN demonstrates high forecasting accuracy for velocity, temperature, and concentration profiles, which minimizes prediction errors while improving the analysis process of Williamson nanofluid flow across a moving wedge.
- ➢ Fluid velocities rise when β enhances while velocity decelerates when βreduces because the parameter increase affects both boundary layer thinness and velocity gradients.
- ➢ Radiative parameter R that leads to improved radiative heat transfer and therefore magnifies temperatures and enlarges thermal boundary layer thickness, but decreases when R values diminish.
- ➢ The elevation or reduction of Nt causes particles to migrate with greater or lesser intensity, which affects surface concentration levels and concentration gradient distributions, respectively.
- ➢ The Schmidt Number (Sc) moderates mass diffusion as it strengthens concentration gradients alongside reducing the solutal boundary layer extent at high values, but facilitates molecular diffusion at low Sc values.
- ➢ The research enhances fluidic system heat and mass transfer optimization by virtue of improved knowledge attainment concerning non-Newtonian nanofluid behavior under complex flow conditions.

Future studies can extend this model to three-dimensional and unsteady MHD Williamson nanofluid flows with variable magnetic and porous conditions. Adding non-Fourier heat flux, variable properties as a function of temperature, and nanoparticle shape effects will add physical realism. Generalization and interpretability can be further improved using higher-level AI paradigms such as deep learning or physics-informed neural networks (PINNs). Additionally, coupling this computational model with experimental verification and multi-objective optimization algorithms will add value to its application in biomedical, aerospace, and industrial applications of heat-transfer systems.

Limitations:

- ➢ Current computational analysis is restricted to a steady, two-dimensional laminar flow around a translating wedge, excluding unsteady, three-dimensional, and transient behaviors possible in practical situations.
- ➢ Homogeneous–heterogeneous reactions were simplified to first-order processes with no activation energy and nonlinear kinetics.
- ➢ Additionally, nanoparticle interactions and aggregation influencing effective viscosity and thermal conductivity were excluded.
- ➢ The developed ANN model single hidden-layer Levenberg–Marquardt network, delivers a satisfactory prediction but may fall short for highly nonlinear systems.

Acknowledgement: This work was supported by the Korea Institute of Energy Technology Evaluation and Planning (KETEP) and the Ministry of Trade, Industry & Energy (MOTIE) of the Republic of Korea (No. RS-2025-02315209).

Funding Statement: This work was supported by the Korea Institute of Energy Technology Evaluation and Planning (KETEP) and the Ministry of Trade, Industry & Energy (MOTIE) of the Republic of Korea (No. RS-2025-02315209).

Author Contributions: Conceptualization, Adnan Ashique and Nehad Ali Shah; Methodology, Usman Afzal, Yazen Alawaideh and Sohaib Abdal; Software, Adnan Ashique, Nehad Ali Shah and Usman Afzal; Validation, Nehad Ali Shah and Jae Dong Chung; Formal analysis, Usman Afzal, Yazen Alawaideh and Sohaib Abdal; Resources, Jae Dong Chung; Supervision, Jae Dong Chung; Writing—original draft, Adnan Ashique, Usman Afzal and Yazen Alawaideh; Writing—review & editing, Nehad Ali Shah, Sohaib Abdal, and Jae Dong Chung. All authors reviewed the results and approved the final version of the manuscript.

Availability of Data and Materials: The data that supports the findings of this study are available from the corresponding author upon reasonable request.

Ethics Approval: Not Applicable.

Conflicts of Interest: The authors declare that they have no conflicts of interest to report regarding the present study.

Nomenclature

Symbol	Name
R	Thermal radiation parameter
Cf_x	Skin friction
ρ	Density
k	Thermal conductivity
$q_r{}^{**}$	Radiative heat flux
Nu_x	Nusselt number
ϑ	Kinematic viscosity
(u, v)	Velocity components
Nb	Brownian motion parameter
D_T	Diffusion coefficient of thermophoresis
α	Thermal diffusivity
Ec	Eckert's number
Nt	Thermophoretic parameter
Bi	Biot number
(x, y)	Cartesian coordinate components
Nb	Brownian motion parameter
We	Weissenberg number
Sc_c	Schmidt number
Sh_x	Sherwood number
D_B	Brownian diffusion
k_d, k_s	The reaction rate constant

References

1. Wang J, Khan MI, Khan WA, Abbas SZ, Khan MI. Transportation of heat generation/absorption and radiative heat flux in homogeneous-heterogeneous catalytic reactions of non-Newtonian fluid (Oldroyd-B model). Comput Meth Programs Biomed. 2020;189:105310. doi:10.1016/j.cmpb.2019.105310.
2. Salahuddin T, Fatima G, Awais M, Khan M, Al Awan B. Adaptation of nanofluids with magnetohydrodynamic Williamson fluid to enhance the thermal and solutal flow analysis with viscous dissipation: a numerical study. Results Eng. 2024;21(3):101798. doi:10.1016/j.rineng.2024.101798.
3. Salahuddin T, Awais M. Thermal and solutal transport by Cattaneo-Christov model for the magnetohydrodynamic Williamson fluid with joule heating and heat source/sink. Heliyon. 2024;10(7):e29228. doi:10.1016/j.heliyon.2024.e29228.
4. Sankari MS, Rao ME, Shams ZE, Algarni S, Sharif MN, Alqahtani T, et al. Williamson MHD nanofluid flow via a porous exponentially stretching sheet with bioconvective fluxes. Case Stud Therm Eng. 2024;59(11–12):104453. doi:10.1016/j.csite.2024.104453.
5. Vieru D, Zafar A. Some Couette flows of a Maxwell fluid with wall slip condition. Appl Math Inf Sci. 2013;7(1):209–19. doi:10.12785/amis/070126.
6. Bilal Arain M, Ijaz N, Hu J. Insight into acoustic wave-driven gas bubble dynamics in Williamson's fluid. J Mol Liq. 2024;394(5):123752. doi:10.1016/j.molliq.2023.123752.

7. Nadeem S, Ishtiaq B, Alzabut J, Ghazwani HA. Entropy generation for exact irreversibility analysis in the MHD channel flow of Williamson fluid with combined convective-radiative boundary conditions. Heliyon. 2024;10(4):e26432. doi:10.1016/j.heliyon.2024.e26432.
8. Shafiq A, Mebarek-Oudina F, Sindhu TN, Abidi A. A study of dual stratification on stagnation point Walters' B nanofluid flow via radiative Riga plate: a statistical approach. Eur Phys J Plus. 2021;136(4):407. doi:10.1140/epjp/s13360-021-01394-z.
9. Sreedevi P, Reddy PS. Thermally radiative nanofluid heat transfer analysis inside a closed chamber with gyrotactic microorganisms. Int J Numer Meth Heat Fluid Flow. 2024;34(12):4206–32. doi:10.1108/hff-02-2024-0146.
10. Mezaache A, Mebarek-Oudina F, Vaidya H, Fouad Y. Heat transfer analysis of nanofluid flow with entropy generation in a corrugated heat exchanger channel partially filled with porous medium. Heat Trans. 2024;53(8):4625–47. doi:10.1002/htj.23149.
11. Fares MN, AL-Saad M, Almutter HHJ, Jasim DJ, Ali Fazilati M, Salahshour S, et al. Two-phase analysis of heat transfer of nanofluid flow in a wavy channel heat exchanger: a numerical approach. Int J Thermofluids. 2024;23:100786. doi:10.1016/j.ijft.2024.100786.
12. Seethamahalakshmi V, Venkata Kalyani U, Padma A, Nagalakshmi PSS, Ramana Reddy GV, Ganteda C, et al. Effects of mass transfer and MHD Casson nanofluid heat transfer on thermophoresis at stagnation point. Case Stud Therm Eng. 2025;69(3):105775. doi:10.1016/j.csite.2025.105775.
13. Mehboob J, Ellahi R, Sait SM, Akbar NS. Optimizing bioconvective heat transfer with MHD Eyring-Powell nanofluids containing motile microorganisms with viscosity variability and porous media in ciliated microchannels. Int J Numer Meth Heat Fluid Flow. 2025;35(2):825–46. doi:10.1108/hff-11-2024-0838.
14. Nandini M, Hanumagowda BN, Saini G, Varma SVK, Tawade JV, Satpute NV, et al. Non-linear thermal radiation impacts on MHD nanofluid flow in a rotating channel with Darcy-forccheimer model: an entropy analysis. J Radiat Res Appl Sci. 2025;18(1):101228. doi:10.1016/j.jrras.2024.101228.
15. Suma UK, Billah MM, Khan AR, Hoque KE. Magnetohydrodynamic mixed convective heat transfer augmentation in a rectangular lid-driven enclosure with a circular hollow cylinder utilizing nanofluids. Int J Thermofluids. 2025;25(4):101014. doi:10.1016/j.ijft.2024.101014.
16. Syam MM, Alkhedher M, Syam MI. Thermal and hydrodynamic analysis of MHD nanofluid flow over a permeable stretching surface in porous media: comparative study of Fe_3O_4, Cu, and Ag nanofluids. Int J Thermofluids. 2025;26(3):101055. doi:10.1016/j.ijft.2025.101055.
17. Madhu J, Saadeh R, Karthik K, Varun Kumar RS, Naveen Kumar R, Punith Gowda RJ, et al. Role of catalytic reactions in a flow-induced due to outer stationary and inner stretched coaxial cylinders: an application of Probabilists' Hermite collocation method. Case Stud Therm Eng. 2024;56(2):104218. doi:10.1016/j.csite.2024.104218.
18. Ajithkumar M, Kuharat S, Anwar Bég O, Sucharitha G, Lakshminarayana P. Catalytic effects on peristaltic flow of Jeffrey fluid through a flexible porous duct under oblique magnetic field: application in biomimetic pumps for hazardous materials. Therm Sci Eng Prog. 2024;49(4):102476. doi:10.1016/j.tsep.2024.102476.
19. Thenmozhi D, Eswara Rao M. Predictor-corrector FDM analysis of MHD Darcy-Forchheimer flow of a micropolar fluid with viscous dissipation and heterogeneous-homogeneous. Propuls Power Res. 2024;13(2):257–72. doi:10.1016/j.jppr.2023.12.002.
20. Hasan N, Saha S. Effects of internal heat production and Joule heating on MHD conjugate mixed convection and entropy production inside a thermally non-homogeneous cooling system. Ann Nucl Energy. 2024;206(6):110671. doi:10.1016/j.anucene.2024.110671.
21. Syam MM. Thermal and fluid behavior of nanofluids over a rotating disk: influence of Darcy-Forchheimer and slip conditions. Int J Thermofluids. 2025;28(2):101316. doi:10.1016/j.ijft.2025.101316.
22. Ur Rehman K, Shatanawi W, Çolak AB. Neural networking-based analysis of heat transfer in MHD thermally slip Carreau fluid flow with heat generation. Case Stud Therm Eng. 2024;54(1):103995. doi:10.1016/j.csite.2024.103995.
23. Ullah H, Alqahtani AM, Raja MAZ, Fiza M, Ullah K, Omer ASA, et al. Numerical treatment based on artificial neural network to Soret and Dufour effects on MHD squeezing flow of Jeffrey fluid in horizontal channel with thermal radiation. Int J Thermofluids. 2024;23(2):100725. doi:10.1016/j.ijft.2024.100725.

24. Assiri TA, Gul T, Khan Z, Muhammad T, Abdualziz Alhabeeb S, Ali I. Artificial neural networks strategy to analyze the magnetohydrodynamics Casson-Maxwell nanofluid flow through the cone and disc system space. Int J Heat Fluid Flow. 2024;107(1):109406. doi:10.1016/j.ijheatfluidflow.2024.109406.
25. Bairagi T, Jahid Hasan M, Hudha MN, Azad AK, Rahman MM. Artificial neural network (ANN) analysis on thermophysical properties of magnetohydrodynamics flow with radiation in an arc-shaped enclosure with a rotating cylinder. Heliyon. 2024;10(7):e28609. doi:10.1016/j.heliyon.2024.e28609.
26. Iqbal J, Abbasi FM, Ali I. Heat transfer analysis for magnetohydrodynamic peristalsis of Reiner-Philippoff fluid: application of an artificial neural network. Phys Fluids. 2024;36(4):041914. doi:10.1063/5.0207600.
27. Shafiq A, Çolak AB, Sindhu TN, Al-Mdallal QM, Abdeljawad T. Estimation of unsteady hydromagnetic Williamson fluid flow in a radiative surface through numerical and artificial neural network modeling. Sci Rep. 2021;11(1):14509. doi:10.1038/s41598-021-93790-9.
28. Atif SM, Hussain S, Sagheer M. Heat and mass transfer analysis of time-dependent tangent hyperbolic nanofluid flow past a wedge. Phys Lett A. 2019;383(11):1187–98. doi:10.1016/j.physleta.2019.01.003.
29. Zaman SU, Aslam MN, Riaz MB, Akgul A, Hussan A. Williamson MHD nanofluid flow with radiation effects through slender cylinder. Res Eng. 2024;22(11):101966. doi:10.1016/j.rineng.2024.101966.
30. Nasir M, Ali ABM, Anwar T, Benabdallah F, Kallel M, Younis F, et al. Impact of liquid hydrogen in stagnation-point flow of hydromagnetic Williamson nanomaterial configured by a stretched vertical wedge featuring nonlinear chemical reaction. Case Stud Therm Eng. 2025;75(10):107122. doi:10.1016/j.csite.2025.107122.
31. Ahmad K, Hanouf Z, Ishak A. MHD Casson nanofluid flow past a wedge with Newtonian heating. Eur Phys J Plus. 2017;132(2):87. doi:10.1140/epjp/i2017-11356-5.
32. Venkateswarlu S, Hari Babu B, Veera Krishna M. Effects of heat generation and absorption on thermal radiative MHD flow of chemically reacting Casson nanofluids over a wedge. Case Stud Therm Eng. 2025;65(3):105637. doi:10.1016/j.csite.2024.105637.